Chapter 4
Chalcopyrite Quantum Wells and Dots in Solar-Cell Applications

Esa Räsänen, Sascha Sadewasser, Sebastian Lehmann, and David Fuertes Marrón

Abstract Chalcopyrite structures are promising candidates for efficient advanced solar cells in thin-film technology. Here we discuss the nanostructuring approach to thin-film photovoltaics and introduce the benefits and challenges of chalcopyrite materials for that purpose. We focus on chalcopyrite quantum wells and quantum dots by describing in detail the growth procedure as well as the theoretical modeling of the obtained structures. We demonstrate that both quantum wells and dots have, in principle, desirable characteristics for applications in photovoltaics.

1 Introduction

1.1 Chalcopyrite Structures in Thin-Film Photovoltaics

The trade-off between production costs and energy conversion efficiency determines the acceptance of photovoltaic (PV) technologies in the market. Chalcopyrite-based solar cells belong to thin-film (TF) approaches to PV.

E. Räsänen (✉)
Department of Physics, Tampere University of Technology, FI-33101 Tampere, Finland
e-mail: esa.rasanen@tut.fi

S. Sadewasser
International Iberian Nanotechnology Laboratory (INL), Avenida Mestre José Veiga, 4715-330 Braga, Portugal
e-mail: sascha.sadewasser@inl.int

S. Lehmann
Solid State Physics, Lund University, Box 118, S-22100 Lund, Sweden
e-mail: Sebastian.Lehmann@ftf.lth.se

D. Fuertes Marrón
Instituto de Energía Solar, ETSIT, Universidad Politécnica de Madrid, Ciudad Universitaria, 28040 Madrid, Spain
e-mail: dfuertes@ies-def.upm.es

X. Wang and Z.M. Wang (eds.), *High-Efficiency Solar Cells: Physics, Materials, and Devices*, Springer Series in Materials Science 190, DOI 10.1007/978-3-319-01988-8_4,
© Springer International Publishing Switzerland 2014

As such, and in contrast to wafer-based PV, the technological strategy has been to minimize the fabrication costs, largely associated to material requirements, while maintaining a reasonable efficiency record from the corresponding devices. The recent history of PV has shown the success of TF approaches, specifically that based on CdTe, with regard to positioning itself as a major player in the industrial sector [1].

Among TF technologies, however, CdTe is neither the most efficient type of device nor the one with the largest potential for improving its performance. Comparing the best small-area devices, those based on chalcopyrites are currently ahead of their CdTe counterparts by two percentage points. Furthermore, the best small-area chalcopyrite device is only one decimal point behind the best wafer-based polycrystalline Si solar cell [2]. Efficiency appears as a robust and objective indicator of the quality and the chances a given technology is capable of in terms of market acceptance. Considering efficiency as an indicator alone, it might then be tempting to imagine a scenario where chalcopyrite-based PV is a direct competitor of crystalline Si. However, such a comparison is unfair, and the market acceptance is nowadays largely set by the price of Si-based Watt-peak (Wp) as reference, currently as low as $0.5/Wp [3]. Like for any other commercial product, the financial analysis of production costs is normally subject to market-driven fluctuations and biases of different nature affecting, for instance, the price of raw materials, the global economic scenario, and large-scale dumping strategies of significant playmakers. All of them are largely unpredictable in the long term. Whether the price of Si-based Wp will remain low or not is not predictable with certainty, although the history generally says that the price of technology is essentially a monotonically decreasing function of time.

Any alternative PV technology able at most to approximately level off poly-Si in terms of cost and efficiency is therefore not expected to have a significant impact on the market acceptance. It is necessary to go beyond that, either in cost, in efficiency or in both. As material scientists, we will just focus here on the efficiency issue. What can be done in this respect? On the road to higher efficiencies there are two main issues to be addressed by TF technologies:

(1) for a technological process of choice, the upscaling from small up to large module areas;
(2) a breakthrough of a new device concept demonstrating improved efficiencies superior to those of Si solar cells.

The former is a specific problem of all TF technologies related to a large extent to monolithic integration of cells into modules in a single processing step. No such problem affects wafer-based PV, where module assembly follows after individual cell sorting. In addition, to ensure homogeneity as required in the fabrication over large areas of films comprised within the device structure as thin as a few tens of nm is not trivial. As a matter of fact, the large gap between highest performances of chalcopyrite-based modules (15 %) and small cells (over 20 %) is to a large extent related to losses associated with monolithic interconnection and inhomogeneity. One may consider upscaling merely as a technological issue: independently of the

inner structure of the device and its performance, it is basically an engineering task to find the way to grow homogeneous layers and to reduce resistive losses. Something different applies to a new device concept.

In this respect, nanotechnology appears as the key to unlock many of the barriers imposed on conventional device architectures that limit their performance. Most of the device concepts belonging to the so-called third-generation PV [4] include nanotechnology in one way or another: quantum wells and quantum dots, multi-color absorbers and intermediate bands, multi-exciton generation and hot carriers, plasmonic enhancement, and light trapping; all of these are examples in which nanodimensional structures are foreseen as ingredients of novel solar cells. A general consensus seems to exist stating that it is through the incorporation of nanostructures how solar cells can surpass the limiting efficiencies imposed by the Shockley–Queisser limit [5].

Before entering the discussion in the next sections on how nanostructures can in principle boost efficiencies, it is also worth mentioning that nanotechnology is expected to play an important role not only in efficiency lift-off but also in reducing processing costs of functional cells. Non-vacuum deposition processes represent a significant advantage in terms of reduced processing costs in comparison to conventional evaporation or sputtering processes. Non-vacuum fabrication is normally based on rapid thermal processing of precursors that utilize inks consisting of emulsions formed by colloidal nanocrystals of the active absorber material in a dispersing medium [6–8]. In addition, this type of material can be used in either organic/inorganic composites [9, 10] or in fully inorganic structures, like porous TiO_2/Cu(In,Ga)S_2-nanocrystal injection cells [11, 12]. These type of processes are currently under development, and they still have to demonstrate whether a sufficient level of device performance, at least comparable to vacuum-based devices, is attainable.

1.2 Nanostructuring Approach: Techniques and Challenges

There has been an increasing number of contributions related to the growth and characterisation of chalcopyrite nanocrystals in recent years (see [13] and references therein). By far, the most of the literature on the topic has considered approaches based on wet chemistry and solvothermal methods, whereby colloidal suspensions and inks are produced for non-vacuum growth processes of conventional devices. Such "wet" processes have resulted in a variety of nanoshapes, including cubes, rods, whiskers, spheres, polyhedra, and beads, also provided with various coatings in subsequent chemical processes.

On the other hand, novel device architectures including nanostructured materials will require the incorporation of nanostructures into solid-state matrices—a difficult task with scarce related literature [9, 10, 13–18].

In principle, conventional deposition methods like molecular beam epitaxy (MBE) or metal-organic vapor phase epitaxy (MOVPE) can be employed for the

growth of chalcopyrite materials and nanostructures, in a similar fashion as used for III–V and II–VI compounds. Such methods allow fine control on the deposition parameters and growth of single crystals in the form of epitaxial layers, when substrates are appropriately selected. Heteroepitaxy is the method of choice for the growth of quantum wells. It can also be used for the growth of three-dimensional nanocrystals acting as quantum dots and permits control between Volmer–Weber and Stranski–Krastanov growth modes. The heteroepitaxy approach will be discussed in the next sections for the cases of quantum dots and wells.

Borrowing methods from wafer-based technologies, however, adds little value by itself to the main advantage of chalcopyrites for PV applications. When speaking of TF-PV one is implicitly speaking of microcrystalline (even amorphous) materials as active layers. The tolerance of such materials to the presence of numerous defects in the crystal lattice must be significant if operative devices can be constructed from them. Such tolerance is well known from devices made of chalcopyrites and CdTe in the form of microcrystalline TFs, devices which do not count with single-crystalline counterparts outperforming them like in the case of III–V, II–VI, or group-IV-based solar cells. It is also of interest to explore ways of incorporating nanostructured material without losing the inherent flexibility of processing materials not too demanding in terms of crystallinity and perfection.

In fact, the nature of chalcopyrite compounds makes them relatively easy to incorporate as nanostructures into certain binary or multinary semiconductors with which they share atomic species, even in the form of microcrystalline layers. Such an approach has been demonstrated before [17, 18], and appears particularly suitable as it can be implemented with standard deposition methods like those employed in industrial scale production. The method profits from the well-known band gap anomaly of ternary (and higher order alloy) compounds of the type I–III–VI_2 with respect to their related II–VI binaries [19]. The anomaly refers to a significant reduction in the value of the band gap observed when comparing I–III–VI_2 compounds with their II–VI relatives, e.g. $CuGaS_2$ vs. ZnS, or even with III_2VI_3 compounds like Ga_2S_3. If the two elements contained in the binary compound (to act as barrier, with a large gap) are all included in the ternary compound (to act, e.g., as quantum dot with a lower gap), pulsed provision of the third species in the ternary may serve as a switch for the deposition of dot and barrier materials, alternatively. Furthermore, use can be made of metallic precursors, like copper, in order to separate "nanostructuring" from "embedding" mechanisms. The size and distribution of nanoscopic precursors on the surface acting as substrate (not necessarily monocrystalline) will determine the dimensions and distribution of the semiconducting nanostructure when processed chemically, whereas the deposition method (chemical deposition, physical evaporation or thermal annealing) will control the simultaneous formation of the ternary compound and the embedding of the nanostructure into the selected matrix compound. Furthermore, the process can be optimized as to yield bare nanostructures instead of buried ones, as to grow selectively on patterned surfaces and to scale the process from nano-, to meso- up to macroscopic dimensions [17, 18].

Regardless of the methods in use for the growth of active material and geometries foreseen, little impact would be expected from nanostructured chalcopyrites if evidences of quantum confinement could not be demonstrated. Experimental evidence of size-dependent light emission in chalcopyrite nanocrystals in the form of colloidal suspensions has been reported though [20–23], opening the door to the incorporation of electronic confining effects into chalcopyrite-based devices. It is worth mentioning at this point that optical response of nanostructures is a necessary property for any type of operative photovoltaic device based on the action of such nanostructures as light absorbers—not only in terms of light absorption but, perhaps most importantly, in terms of light emission as result of carrier recombination mechanisms. As a matter of fact, luminescence is the key factor determining ultimately whether such a device would operate in the radiative limit and thus if maximum efficiencies can be expected from it.

In the following sections we will focus on two particular aspects of chalcopyrite-based nanostructures with regard to new device architectures and possible ways to improve their performance over that of current record holders. We will describe the growth and properties of quantum wells and quantum dots, highlighting the main properties and issues raising up from quantum confinement effects in one and three dimensions and discussing ways to exploit such effects in operating devices.

2 Chalcopyrite Quantum Wells

2.1 Growth Procedure

Quantum-well structures are typically grown using MBE or MOVPE. Both methods allow for a high level of compositional and spatial control of the deposited layers. While quantum-well structures are frequently realized using III–V or II–VI material systems, reports of chalcopyrite-based quantum wells are very limited [24, 25]. Chalcopyrite-based quantum-well superlattices can result in improved excitonic absorption compared to bare films, leading to a potential enhancement in efficiency figures. For these studies, several different $CuInSe_2$ and $CuGaSe_2$ quantum well samples have been grown in a commercial MOVPE system (AIXTRON AIX200SC). Various metal-organic compounds were used as precursors for copper, gallium, indium, and selenium, namely: cyclopentadienyl-coppertriethylphosphine (Cp-CuTEP), triethylgallium (TEGa), trimethylindium (TMIn), and ditert-butylselenide (DTBSe). Epiready GaAs:Zn (100) wafers (EpiChem) were used as substrates.

Prior to growth, the substrates were annealed in hydrogen atmosphere at a temperature of 650 °C before setting the growth temperatures to $T_{sub} = 500$ °C for $CuInSe_2$ and $T_{sub} = 570$ °C for $CuGaSe_2$, respectively. Samples were grown with a ratio of [Cu]/[Ga] ≈ 0.9 for the nominal value of the incoming precursor fluxes which corresponds to slightly Cu-poor conditions. The validity of this

procedure is based on the rather forgiving chemistry of the considered chalcopyrite materials for Cu-poor off-stoichiometries. Further, it assures the suppression of parasitic $Cu_{1-x}Se$ phase formation [26, 27]. Details of the growth conditions and its optimization can be found elsewhere [28, 29].

For this exploratory study of the possibility to grow chalcopyrite quantum wells, several samples were prepared. For comparative purposes, single $CuInSe_2$ or $CuGaSe_2$ layers were grown on the GaAs(100) substrate as references using identical growth conditions as used for multilayer structures. The final layer thickness of these single layer samples was about 350 nm. Those samples served as references in order to compare material properties of thick layers with the thin ones as prepared in the multilayer stack samples. A multilayer stack sample was grown consisting of 50 nm layers with the following sequence GaAs/$CuGaSe_2$/$CuInSe_2$/$CuGaSe_2$. This stack provides a $CuInSe_2$ well surrounded by $CuGaSe_2$ barriers. For this sample, the top $CuGaSe_2$ layer was grown at $T_{sub} = 500$ °C instead of the usual 570 °C, in order to avoid exposure of the $CuInSe_2$ quantum well to a temperature higher than its growth temperature. However, for photoluminescence experiments, this stack sequence is not optimal, as the light emitted from the $CuGaSe_2$ bottom barrier can be reabsorbed by the $CuInSe_2$ well. Therefore, an additional multilayer sample was fabricated with a sequence of GaAs/$CuInSe_2$/$CuGaSe_2$/$CuInSe_2$.

One important difference between chalcopyrite semiconductors and widely used III–V semiconductors is the process of doping. While for III–V semiconductors, active extrinsic doping is necessary and typically applied during the growth, the Cu-chalcopyrites are not extrinsically doped. For most of the investigated growth processes including MBE and MOVPE chalcopyrites normally show p-type conductivity. This behavior is mainly explained by the spontaneous formation of intrinsic defects during preparation. It leads to a net excess of Cu vacancies and thus to the commonly reported conductivity behavior [30].

The multilayer structure was analyzed using energy dispersive X-ray spectroscopy (EDX) in a transmission electron microscope (TEM), to study interdiffusion phenomena of In and Ga between the quantum well and the barrier layers. Figure 4.1 shows the elemental distribution (intensity of the L-emission) of Cu, Ga, In, Se, and As through the layer stack. The interface between the GaAs substrate and the chalcopyrite layer stack is clearly resolved. While Cu and Se appear homogeneously distributed throughout the entire layer stack, In and Ga exhibit an inhomogeneous distribution. Both elements, In and Ga, are observed in all three layers of the stack, despite the nominal growth of a $CuGaSe_2$/$CuInSe_2$/$CuGaSe_2$ sequence. This indicates a significant diffusion of In and Ga on the cation sublattice at the growth temperatures. Nevertheless, the In concentration in the center of the layer stack is higher compared to the surrounding layers. In contrast, the Ga concentration is higher in the embedding layers compared to the centered one. This can be more clearly seen in the extracted line profiles of the elemental distribution along the growth direction of the layer stack as displayed in Fig. 4.1g. This elemental distribution was also independently confirmed by secondary ion mass spectrometry (SIMS) measurements [25]. In addition to the

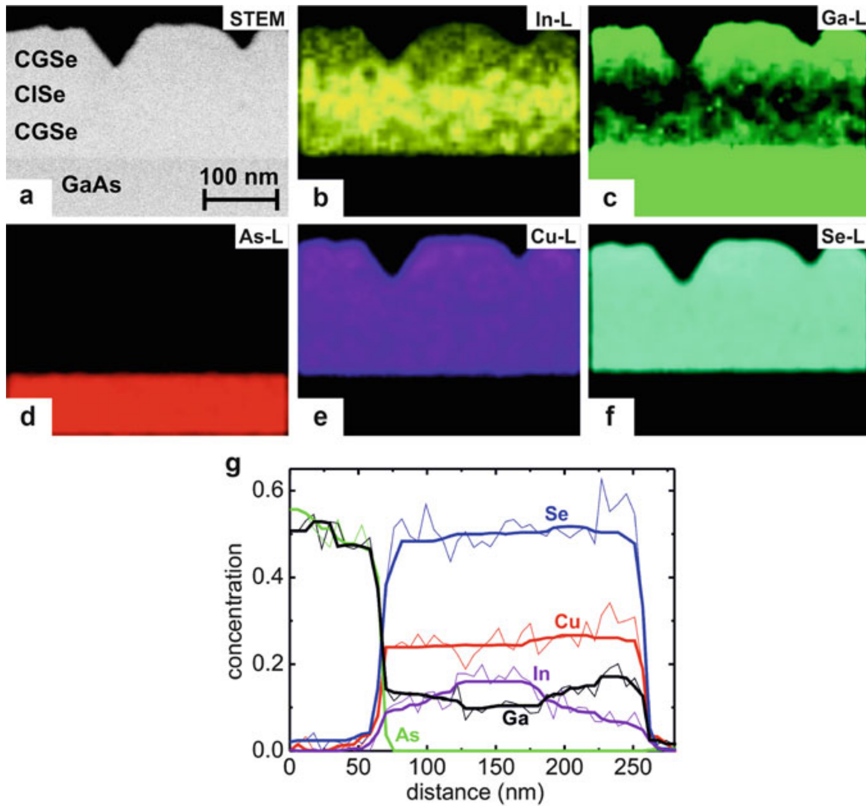

Fig. 4.1 (**a**) Scanning TEM image of a GaAs/$CuGaSe_2$/$CuInSe_2$/$CuGaSe_2$ multilayer stack. EDX mappings showing the intensity of the L-emission lines of the elements (**b**) In, (**c**) Ga, (**d**) As, (**e**) Cu, and (**f**) Se. The relative elemental concentration is proportional to the intensity. (**g**) Line profiles of the elemental distribution along the growth direction obtained from the EDX maps. Despite a strong interdiffusion of In and Ga throughout the three chalcopyrite layers, the center $CuInSe_2$ layer shows a significantly higher In concentration than the surrounding $CuGaSe_2$ layers. Figures adapted from [24, 25]

variation of In and Ga along the growth direction of the multilayer stack, an inhomogeneous distribution in the lateral direction can also be observed. Spots of about 10–30 nm size with an increased In content can clearly be observed from Fig. 4.1b.

2.2 *Modeling of the Multilayer Sample*

In order to assess quantum confinement in the $CuInSe_2$ layer, the multilayer stack has to be modeled. In particular, the band diagram of the stack is needed. The depth profile of the Cu(In,Ga)Se_2 material composition can be extracted from the EDX

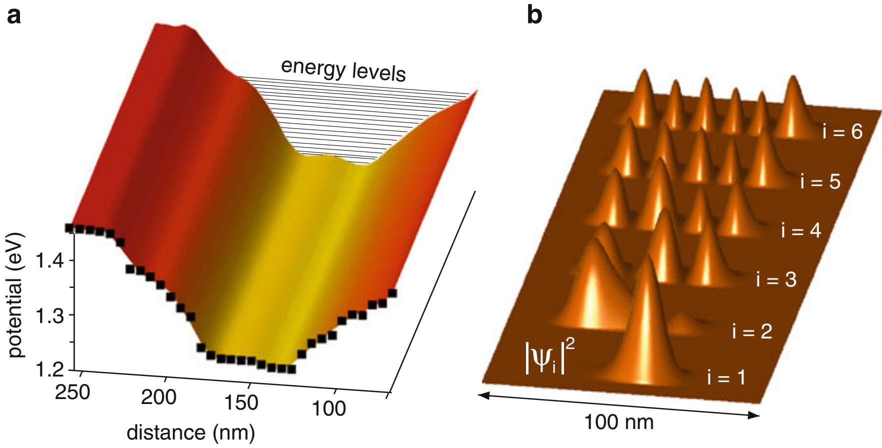

Fig. 4.2 (**a**) Quantum-well potential obtained through polynomial fitting to the measured profile (*squares*) and the first quantized energy levels (*lines*). (**b**) Squares of the first six eigenstates confined in the potential. Figures adapted from [25]

results shown in Fig. 4.1g. The band gap E_g of $CuIn_{1-x}Ga_xSe_2$ depends on the composition x as

$$E_g(x) = (1-x)E_g(CuInSe_2) + xE_g(CuGaSe_2) - bx(1-x), \qquad (4.1)$$

where $b = 0.21$ is the bowing factor [31]. The band offset between $CuGaSe_2$ and $CuInSe_2$ is expected to evolve only in the conduction band. Hence, a $CuInSe_2$ well is formed for electrons between $CuGaSe_2$ barriers. Here we neglect the small valence band offset between $CuGaSe_2$ and $CuInSe_2$. Now, the composition profile x for the In/Ga ratio can be obtained as a function of position. Further, using (4.1) we can obtain the band gap as function of position, see the square points in Fig. 4.2a. This result can now be applied as a model potential in order to calculate the quantized energy levels.

2.3 *Quantum Confinement*

The measured profile in Fig. 4.2a (square points) is modeled by fitting a one-dimensional polynomial in the 17th order. The result of the fit is taken as an external confining potential for the electronic states in the quantum well. The energy levels of the quantized states are then obtained by solving the (one-dimensional) single-particle Schrödinger equation. The effective-mass approximation [32] with material parameters $m^* = 0.1m_e$ and $\varepsilon = 5\varepsilon_0$ was used.

As shown in Fig. 4.2a (solid lines), several (∼20) confined states were obtained. Within a two- or three-dimensional model the number of confined states would be

even larger due to additional symmetry leading to degenerate states. Figure 4.2b shows the squares of the first six eigenstates confined in the quantum-well model. The first state clearly localizes at the global minimum of the potential, whereas the second state localizes in the neighboring local minimum. The higher states then form a rather regular nodal structure and a pattern of Gaussian-shaped peaks.

In conclusion of this part, distinctive quantum wells can be grown of chalcopyrite materials with the MOVPE technique. Considerable interdiffusion between In and Ga at the interfaces leads to a smooth conduction band profile between the well and the barriers. Theoretical modeling gives clear signatures of quantum confinement in the $CuInSe_2$ well. In the future, more efforts are needed to fabricate smaller $CuInSe_2$ wells as well as multilayer stacks that include several quantum wells. Experimental evidence of electronic confinement for this structure was in fact reported based on modulation spectroscopy results [24].

3 Chalcopyrite Quantum Dots

3.1 Growth Procedure

For the growth of chalcopyrite quantum dots, a variety of different approaches have been reported. Solution-based methods result in colloidal particles, while dry deposition methods have been used to grow nanodots on substrate surfaces, or embedded into a matrix material. Colloidal nanoparticles have been fabricated from solution resulting in different chalcopyrite compounds including $CuInSe_2$, $CuGaSe_2$, and $CuInS_2$ [33–35]. One application for such nanoparticles is their deposition onto a Mo/glass substrate and subsequent sintering of this nanoparticle layer into a thin film [36, 37]. This approach aims at the fabrication of regular thin film devices by a rather cost-effective method. Since this approach does not lead to a high-efficiency solar cell exploiting the quantum effects of the nanoparticles, it is not considered further in this chapter. In other applications of such colloidal nanoparticles the aim is to provide the nanoparticle for an effective absorption of light, possibly covering various parts of the solar spectrum and transfer the excited charge carriers into an electron acceptor material, e.g. TiO_2 [12]. The function of the nanoparticle in this approach is similar to that of dye molecules and such solar cells are called nanoparticle-sensitized solar cells [38]. While the quantum effect can possibly be exploited in these approaches, prototype solar cells have typically low efficiencies and stability is a critical issue also.

The growth of chalcopyrite quantum dots has also been realized following the standard dry deposition methods applied for the growth of III–V quantum dots, namely MBE and MOVPE. MBE growth has been realized for $CuGaSe_2$ on Si(111) substrates. The single elements were evaporated from effusion cells onto the substrate at a temperature of $T_{sub} = 600$ °C and the growth time was set to 10 min. Figure 4.3b shows an overview scanning electron microscopy (SEM)

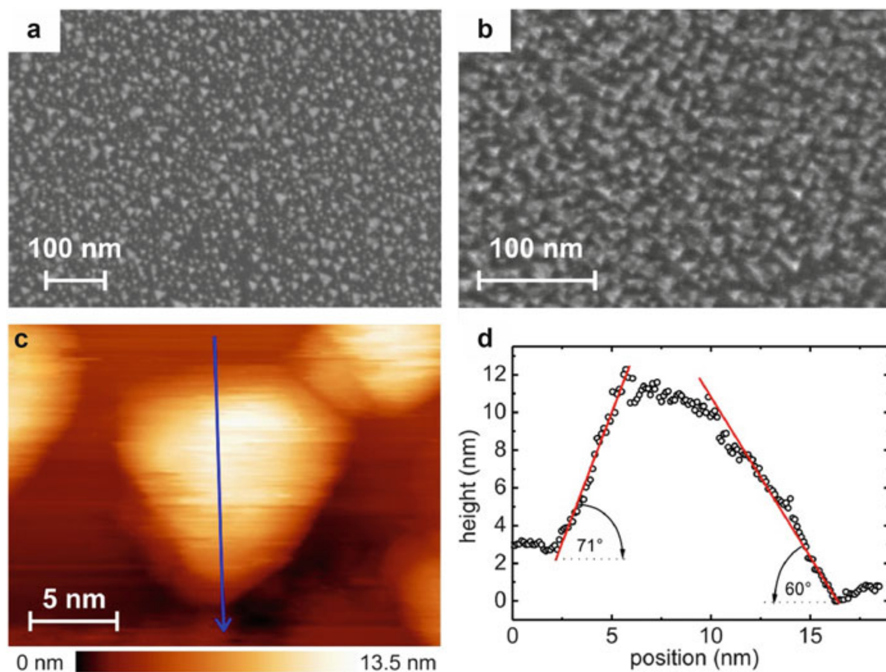

Fig. 4.3 (**a**) SEM *top view* image of $CuInSe_2$ nanodots grown by MOVPE on a Si(111) substrate. (**b**) SEM *top view* image of $CuGaSe_2$ nanodots grown by molecular beam epitaxy on a Si(111) substrate. (**c**) STM image of one individual $CuGaSe_2$ nanodot. (**d**) Height profile of the $CuGaSe_2$ nanodot showing the relevant angles of the side and the facets, as determined from the topography. Figure reproduced with permission from Applied Physics Letters [44]

image of a representative sample after deposition and Fig. 4.3c a scanning tunneling microscopy (STM) image of a single quantum dot. The geometry of the resulting quantum dots was analyzed from an average of numerous STM height profiles, as displayed in Fig. 4.3d. The shape was found to be close to that of a tetrahedron and independently confirmed by transmission electron microscopy. MOVPE has also been successfully used for the preparation of $CuInSe_2$ and $CuGaSe_2$ quantum dots. Figure 4.3a shows an overview image for the growth of a 5 min $CuInSe_2$ deposition onto a Si(111) substrate at $T_{sub} = 500$ °C. This growth was performed in an Aixtron AIX200SC MOVPE using the metal-organic compounds cyclopentadienyltriethylphosphinecopper (CPTPC), trimethylindium (TMIn), triethylgallium (TEGa), and ditertiarybutylselenide (DTBSe). Nanodot growth has been realized over a broad temperature range from 500 to 620 °C for both $CuInSe_2$ and $CuGaSe_2$ materials.

A different growth approach without the requirement of an epitaxial substrate is based on decoupling the nanostructuring step from the reaction step forming the chalcopyrite compound [17, 18]. In a first step, Cu precursors are deposited in a nanostructured way, for example by self-assembly or masks onto an

arbitrary substrate. In the second step, a reactive atmosphere containing i.e. In and Se is supplied to transform the Cu-dots into $CuInSe_2$ dots. As a function of the reaction conditions, the growth can be tuned to deposit a binary matrix material simultaneously to the chemical reaction of converting the Cu precursor dots into chalcopyrite material.

Yet another approach [24] is to embed quantum dots into a wider band gap absorber material, with a growth process as similar as possible to conventional chalcopyrite TF growth. The device structure was designed to lead to a conceptual intermediate band absorber with $CuInS_2$ quantum dots embedded in an In_2S_3 matrix material. This material combination could in principle result in quantum dots entirely surrounded by a higher band gap ($E_g = 2.0$ eV) matrix material. The samples were grown as polycrystalline layers on Mo-coated, Na-free glass (Corning 7059) using physical vapor deposition and a substrate temperature of $T_{sub} = 200$ °C. A metal precursor sequence of In (55 nm)/Cu(1 nm)/In(60 nm)/Cu(1 nm)/In(65 nm)/Cu(1 nm)/In(70 nm) was used during constant supply of sulfur, leading to an overall [Cu]/([Cu] + [In]) ratio of 2–3 at.%. Reference indium sulfide samples without Cu addition were also grown.

3.2 Modeling of Tetrahedral Quantum Dots

Next we turn our attention into theoretical modeling of tetrahedral chalcopyrite quantum dots shown in Fig. 4.3. It is noteworthy that here we do not resort to atomistic ab initio calculations but apply the effective mass approximation [32] and solve the electronic states in a model potential. Recent discussion about the challenges of first-principles calculations on chalcopyrite materials can be found, e.g., in [39, 40] and in references therein. These atomistic approaches to *confined* chalcopyrite nanostructures (such as quantum dots) are particularly challenging as the systems cannot be handled computationally using periodic cells.

As in Sect. 2.3 we apply the effective-mass approximation by assuming that the electrons are near the band minimum, where the band can be approximated as parabolic. In general, the effective mass approximation has a few drawbacks. For example, the space dependence of the effective mass and the dielectric constant in heterostructures can lead to non-parabolicity of the energy bands near $k = 0$ [41]. In practice, however, the effective mass approximation has been successfully used in various electronic-structure calculations on semiconductor (such as GaAs and InAs) quantum dots [42]. Here we use the electron effective mass in the $CuInSe_2$ QD $m^* = 0.09m_0$. As another assumption, the electronic wave functions are not expected to penetrate deep into the matrix material. Hence, we may use the same dielectric constant throughout both the quantum dot and the matrix material, i.e., $\varepsilon = 15.1$ [43].

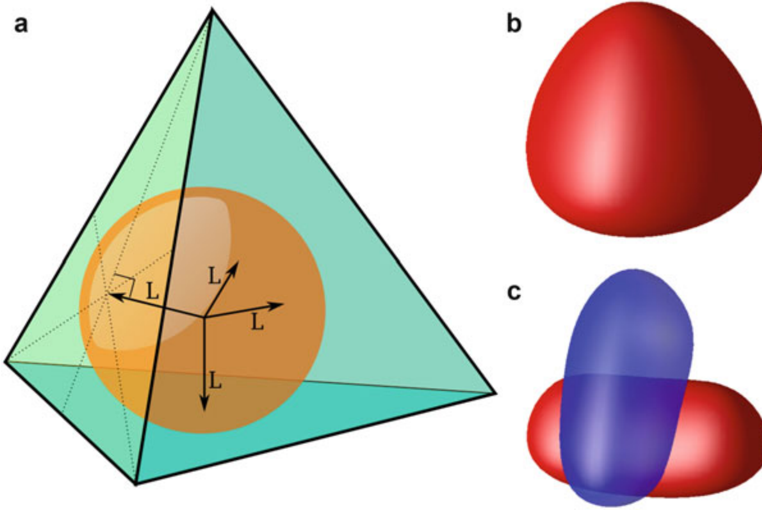

Fig. 4.4 (**a**) Tetrahedral model potential used in the calculations. The distance $L = 4.42$ nm is the radius of the sphere fitting inside the tetrahedron. (**b**, **c**) Eigenfunctions of the lowest and second lowest bound states, respectively, in the system. The *red* and *blue* surfaces correspond to constant values 41 and -41 $\mathrm{nm}^{-3/2}$, respectively. The viewing angle is the same as for the external model potential in (**a**)

Based on the SEM image and the height profile of the quantum dot (Fig. 4.3) we construct a model potential for the electronic confinement in the quantum dot. The external model potential, that essentially accounts for the surroundings of the conduction-band electrons, is given by

$$V_{\mathrm{ext}}(\mathbf{r}) = -V_0 \exp\left[\frac{-(\mathbf{r}\cdot\mathbf{n}_i)^2}{2L^2}\right], \tag{4.2}$$

where $\mathbf{n}_i$ are the normal vectors of the faces of the tetrahedron and L is the radius of the quantum dot, or, more explicitly, it is the radius of the sphere fitting inside the tetrahedron as visualized in Fig. 4.4a.

The radius of the typical grown dot in Fig. 4.3 is approximately $L_{\mathrm{exp}} = 3, \ldots, 4$ nm. The depth of the potential $V_0 = 1.18$ eV is set to be equal to the conduction band offset between the dot and the matrix materials [44]. The Gaussian tail in V_{ext} models the slowly varying confinement at the smooth interface between the quantum dot and matrix regions. On the other hand, the Gaussian form is approximately harmonic close to the dot center; this is a reasonable approximation in view of previous quantum dot studies (for recent combined works of experiment and theory verifying the validity of a harmonic model potential, see, e.g., [42, 45, 46]).

OCTOPUS code package [47] was used in solving the static single-particle Schrödinger equation with the external potential in (4.2). OCTOPUS is a versatile tool for dealing with both static and time-dependent electronic-structure

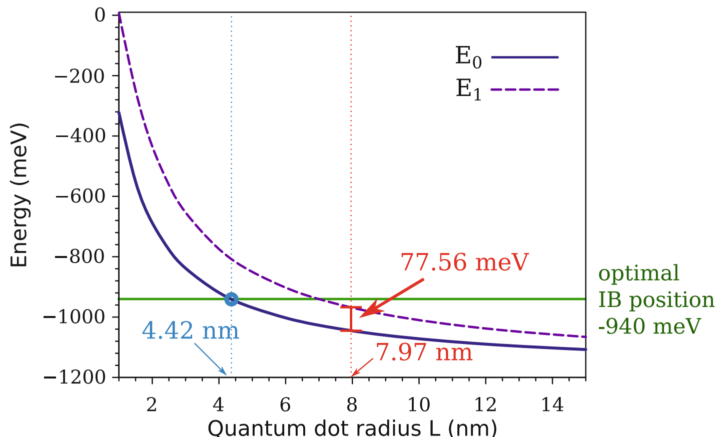

Fig. 4.5 Energies of the first and second electronic states of a $CuInSe_2$ dot in a $CuGaS_2$ matrix as a function of the quantum dot size L [see Fig. 4.4a]. The *solid horizontal line* marks the optimal intermediate-band position corresponding to the radius of 4.42 nm (*left dotted line*). The *right dotted line* marks the maximum size of the quantum dot to satisfy the thermal constraint (see text). The bound-state constraint corresponds the left border of the figure ($\sim$ 1 nm). Figure reproduced with permission from Applied Physics Letters [44]

calculations—especially within the density-functional theory framework—in real space and real time. It is a free software published under the GPL license. Here the grid spacing was $L/70$, leading to about 1,400,000 grid points altogether.

The eigenfunctions of the two lowest bound states are shown in Fig. 4.4b and c, respectively. The lowest state resembles an atomic 1s orbital with a slight tetrahedral deviation, whereas the second lowest state has a planar node across the tetrahedron. The two lowest energy levels as a function of the quantum dot size L are shown in Fig. 4.5 (higher levels omitted in the figure). The energies are compared to the optimal intermediate-band position at -940 meV that can be obtained from the procedure introduced by Luque and Martí [48]. In principle, the optimal position yields maximum efficiency of 61.1 % in concentrated sunlight. This is close to the *overall* maximum of an intermediate-band solar cell that is as high as 63.2 %. In fact, significant recent advances have been achieved in Sn-doped chalcopyrites that show wide-spectrum solar response [49]. Here, the crossing point between the optimal position and the ground-state energy is found at $L_{\mathrm{opt}} = 4.42$ nm. This can be regarded as the optimal size of the quantum dot, which qualitatively agrees very well with the sizes of the grown samples (Fig. 4.3).

Finally, we can verify that the optimal quantum dot size satisfies two important physical constraints. First, the *minimum* dot diameter, ensuring the existence of at least one bound state, is given by [50]

$$D_{\min} = \frac{\pi\hbar}{\sqrt{2m^* \Delta E_{\mathrm{b}}}}, \tag{4.3}$$

and ΔE_b is the energy barrier between the dot and the matrix, i.e., the conduction band offset (electrons) or the valence band offset (holes). For our system this condition yields $L_{min} = 0.94$ nm, which corresponds to the left boundary in Fig. 4.5. On the other hand, the *maximum* quantum-dot size can be estimated from the requirement that the thermal population of the excited states remains small [51]. If we require less than 5 % occupation at room temperature 300 K, the level separation needs to be

$$kT \leq \frac{1}{3}|E_1 - E_0|, \tag{4.4}$$

where E_0 and E_1 are the first two energy levels of the dot. This condition yields $L_{max} = 7.97$ nm marked in Fig. 4.5.

In conclusion of this section, we have constructed a realistic model for the single chalcopyrite quantum dot and have shown that the dot size that yields the optimal efficiency is in qualitative agreement with the grown experimental samples. In addition, the important condition for the existence of a bound state, as well as the thermal condition for the level population, are satisfied. However, application of chalcopyrite quantum dots in an intermediate-band solar cell requires controlled growth of periodic tetrahedral nanodots regarding their size, shape, and structuring.

Acknowledgements This work was supported by the Academy of Finland, the Fortum Foundation, and the European Community's FP7 through the CRONOS project, grant agreement no. 280879.

References

1. Jäger-Waldau, A.: PV-Status Report 2012, p. 28. European Union (2012). Available at http://re.jrc.ec.europa.eu/
2. Green, M.A., Emery, K., Hishikawa, Y., Warta, W., Dunlop, E.: Prog. Photovolt.: Res. Appl. **21**, 1 (2013)
3. Photon International, January 2013, p. 63
4. Green, M.A.: Third Generation Photovoltaics, Advanced Solar Energy Conversion. Springer, New York (2006)
5. Shockley, W., Queisser, H.J.: J. Appl. Phys. **32**, 510 (1961)
6. Guo, Q., Kim, S.J., Kar, M., Shafarman, W.N., Birkmire, R.W., Stach, E.A., Agrawal, R., Hillhouse, H.W.: Nano Lett. **8**, 2982 (2008)
7. Guo, Q., Ford, M., Hillhouse, H.W., Agrawal, R.: Nano Lett. **9**, 3060 (2009)
8. Panthani, M.G., Akhavan, V., Goodfellow, B., Schmidtke, J.P., Dunn, L., Dodabalapur, A., Barbara, P.F., Korgel, B.A.: J. Am. Chem. Soc. **130**, 16770 (2008)
9. Arici, E., Sariciftci, N.S., Meissner, D.: Adv. Funct. Mater. **13**, 165 (2003)
10. Kruszynska, M., Knipper, M., Kolny-Olesiak, J., Borchert, H., Parisi, J.: Thin Solid Films **519**, 7374 (2011)
11. Nanu, M., Schoonman, J., Goossens, A.: Nano Lett. **5**, 1716 (2005)
12. Santra, P.K., Nair, P.V., Thomas, K.G., Kamat, P.V.: J. Phys. Chem. Lett. **4**, 722 (2013)

13. Fuertes Marrón, D.: Thin film technology in intermediate band solar cells: advanced concepts for chalcopyrite solar cells. In: Cristóbal, A.B.., Martí, A., Luque, A. (eds.) Next Generation of Photovoltaics, p. 277. Springer, Berlin (2012)
14. Bodnar, I.V., Gurin, V.S., Molochko, A.P., Solovei, N.P., Prokoshin, P.V., Yumashev, K.V.: Semiconductors **36**, 298 (2002)
15. Bodnar, I.V., Gurin, V.S., Molochko, A.P., Solovei, N.P.: Inorg. Mater. **40**, 797 (2004)
16. Arici, E., Meissner, D., Schäffler, F., Sariciftci, N.S.: Int. J. Photoenergy **5**, 199 (2003)
17. Fuertes Marrón, D., Lehmann, S., Kosk, J., Sadewasser, S., Lux-Steiner, M.Ch.: Mater. Res. Soc. Symp. Proc. **1012**, Y02-07 (2007)
18. Fuertes Marrón, D., Lehmann, S., Lux-Steiner, M.Ch.: Phys. Rev. B **77**, 085315 (2008)
19. Jaffe, J.E., Zunger, A.: Phys. Rev. B **27**, 5176 (1983)
20. Kuo, K.T., Chen, S.Y., Cheng, B.M., Lin, C.C.: Thin Solid Films **517**, 1257 (2008)
21. Li, D., Zou, Y., Yang, D.: J. Lumin. **132**, 313 (2012)
22. Allen, P.M., Bawendi, M.G.: J. Am. Chem. Soc. **130**, 9240 (2008)
23. Hamanaka, Y., Ogawa, T., Tsuzuki, M., Kuzuya, T.: J. Phys. Chem. C **115**, 1786 (2011)
24. Fuertes Marrón, D., Cánovas, E., Levy, M.Y., Martí, A., Luque, A., Afshar, M., Albert, J., Lehmann, S., Abou-Ras, D., Sadewasser, S., Barreau, N.: Sol. Energy Mater. Sol. Cells **94**, 1912 (2010)
25. Afshar, M., Sadewasser, S., Albert, J., Lehmann, S., Abou-Ras, D., Fuertes Marrón, D., Rockett, A.A., Räsänen, E., Lux-Steiner, M.Ch.: Adv. Energy Mater. **1**, 1109 (2011)
26. Mikkelsen, J.C.J.: Ternary phase relations of the chalcopyrite compound $CuGaSe_2$. J. Electron. Mater. **10**, 541–558 (1981)
27. Goedecke, T., Haalboom, T., Ernst, F.: Phase equilibria of Cu–In–Se I.-III. Z. Metallkd. **91**, 622–662 (2000)
28. Bauknecht, A., Siebentritt, S., Albert, J., Lux-Steiner, M.Ch.: J. Appl. Phys. **89**, 4391 (2001)
29. Rega, N., Siebentritt, S., Albert, J., Nishiwaki, S., Zajogin, A., Lux-Steiner, M.Ch., Kniese, R., Romero, M.: Thin Solid Films **480–481**, 286 (2005)
30. Siebentritt, S., Igalson, M., Persson C., Lany, S.: Prog. Photovolt.: Res. Appl. **18**, 390 (2010)
31. Wei, S.-H., Zunger, A.: J. Appl. Phys. **78**, 3846 (1995)
32. See, e.g., Ullrich, C.: In: Marques, M.A.L., Ullrich, C.A., Nogueira, F., Rubio, A., Burke, K., Gross, E.K.U. (eds.) Time-Dependent Density Functional Theory. Lecture Notes in Physics, pp. 271–285. Springer, Berlin (2006)
33. Zhong, H., Li, Y., Ye, M., Zhu, Z., Zhou, Y., Yang, C., Li, Y.: Nanotechnology **18**, 025602 (2007)
34. Peng, S., Liang, Y., Cheng, F., Liang, J.: Sci. China Chem. **55**, 1236–1241 (2012)
35. Panthani, M.G., Akhavan, V., Goodfellow, B., Schmidtke, J.P., Dunn, L., Dodabalapur, A., Barbara, P.F., Korgel, B.A.: J. Am. Chem. Soc. **130**, 16770–16777 (2008)
36. Guo, Q., Kim, S.J., Kar, M., Shafarman, W.N., Birkmire, R.W., Stach, E.A., Agrawal, R., Hillhouse, H.W.: Nano Lett. **8**, 2982 (2008)
37. Guo, Q., Ford, G.M., Hillhouse, H.W., Agrawal, R.: Nano Lett. **9**, 3060 (2009)
38. O'Regan, B., Grätzel, M.: Nature **353**, 737–740 (1991)
39. Vidal, J., Botti, S., Olsson, P., Guillemoles, J.-F., Reining, L.: Phys. Rev. Lett. **104**, 056401 (2010)
40. Oikkonen, L.E., Ganchenkova, M.G., Seitsonen, A.P., Nieminen, R.M.: Phys. Rev. B **86**, 165115 (2012)
41. Burt, M.G.: J. Phys. Condens. Matter **4**, 6651 (1992)
42. For a review, see Reimann, S.M., Manninen, M.: Rev. Mod. Phys. **74**, 1283 (2002)
43. Syrbu, N.N., Bogdanas, M., Tezlevan, V.E., Mushcutariu, I.: Physica B **229**, 199 (1997)
44. Ojajärvi, J., Räsänen, E., Sadewasser, S., Lehmann, S., Wagner, Ph., Lux-Steiner, M.Ch.: Appl. Phys. Lett. **99**, 111907 (2011)
45. Räsänen, E., Saarikoski, H., Harju, A., Ciorga, M., Sachrajda, A.S.: Phys. Rev. B **77**, 041302 (R) (2008)
46. Rogge, M.C., Räsänen, E., Haug, R.J.: Phys. Rev. Lett. **105**, 046802 (2010)

47. Castro, A., Appel, H., Oliveira, M., Rozzi, C.A., Andrade, X., Lorenzen, F., Marques, M.A.L., Gross, E.K.U., Rubio, A.: Phys. Status Solidi (b) **243**, 2465 (2006)
48. Luque, A., Martí, A.: Phys. Rev. Lett. **78**, 5014 (1997)
49. Yang, C., Qin, M., Wang, Y., Wan, D., Huang, F., Lin, J.: Sci. Rep. **3**, 1286 (2013)
50. Bimberg, D., Grundmann, M., Ledentsov, N.N.: Quantum Dot Heterostructures. Wiley, Chichester (1998)
51. Fuertes Marrón, D., Martí, A., Luque, A.: Phys. Status Solidi A **206**, 1021 (2009)